Experimental and CFD scale-up studies for intensified actinide/lanthanide separations

Dimitrios Tsaoulidis†*, Milan Mamtora, Miguel Pineda, Eric S. Fraga, Panagiota Angeli*

Department of Chemical Engineering, University College London, WC1E 7JE, London, UK

*corresponding authors: d.tsaoulidis@surrey.ac.uk, p.angeli@ucl.ac.uk

Abstract

In this paper, systematic studies are performed to identify the parameters that influence the selective separation of actinides from a mixture with lanthanides in small channels. In particular, the separation of dioxouranium metal ions (UO_2^{+2}) from a binary U(VI)/Er(III) mixture in a nitric acid solution by an organic TBP/kerosene (Exxsol D80) phase, relevant to spent nuclear fuel reprocessing is investigated. The effects of parameters such as TBP concentration, organic to aqueous phase flow rate ratio, channel size, and residence time on mass transfer are evaluated, whilst the mass transfer performance in the extraction channels is further analysed using two important hydrodynamic features, i.e. plug formation time and interfacial area to volume ratio. Circular channels with diameters from 1 to 3 mm are used to investigate the effect of scale on the mass transfer characteristics. The importance of the mixing zone on mass transfer is also evaluated. A CFD model is proposed to simulate the mass transfer during plug flow. Using only one experimental point, once the plug has been formed, the model is able to predict extraction percentage with less than 4% difference compared to the experiments.

1. Introduction

Process intensification (PI) design principles can have a large impact on the development of cleaner, more efficient, and economical processes. Intensification of operations involving immiscible liquids such as solvent extractions, separations, reactions, and emulsifications, has gained considerable attention in process engineering [1]. One option for process intensification is the use of small channels, where mass and heat transfer rates are enhanced due to short diffusion lengths and high surface area to volume ratios, leading to improved efficiencies and reduced waste. Compared with conventional extraction equipment (mixer-settlers, pulsed

†current address: Chemical and Process Engineering Department, University of Surrey, GU2 7XH, Guildford, Surrey, UK

columns) or other intensified approaches (e.g. centrifugal extractors), small-scale devices overcome problems such as long residence and mixing times, large footprint, high energy consumption, and large inventories.

In small-scale intensified channels, the flow patterns that are mainly formed vary from parallel to chaotic to segmented flows [2]. Each of the patterns has its own benefits, depending on the application. However, the most widely investigated flow pattern is the segmented (or plug) flow (shown in Fig. 1). In this pattern, one phase forms dispersed droplets (plugs) whose equivalent diameter is larger than the channel diameter, whilst the other phase is continuous (slug) and surrounds the plugs separating them from each other as well as from the channel wall via a thin film. During plug flow, axial mixing is limited, while the circulation patterns that are established within each phase improve radial mixing [3].

One sector that would benefit from the intensification of extraction separations is civil nuclear power generation, where one of the major concerns is the management of the spent nuclear fuel emanating from the nuclear reactor. Aqueous separations based on solvent extraction remain the leading option for spent nuclear fuel reprocessing [4]. They are mainly based on the established PUREX process, where uranium and plutonium are recovered from nitric acid solutions of the spent fuel. Alternative processes to PUREX have also been developed, aiming at recovering additional actinides and lanthanides (GANEX or SANEX) [5, 6]. Lanthanides are divided into two categories, namely lighter and heavier ones depending on their electronic configuration. Due to their high values of neutron-capture cross-section, lanthanides such as erbium, europium, gadolinium, dysprosium, and samarium are added in the control and fuel rods in nuclear reactors. However, heavy lanthanides such as erbium and dysprosium are in supply risk, making their recycle a desirable option [7].

Over the last decade, microchannels have been investigated for applications relevant to spent nuclear fuel reprocessing, radiochemistry, and radionuclide separations [8, 9]. Most of the studies included single-component extractions of lanthanides, actinides or other metallic elements, used as surrogates for radioactive elements. In Table 1, the experimental works that involve mainly actinide and lanthanide separations in microchannels are summarised. A common key finding is the high extraction percentage achieved in short residence times. In addition, the volumes involved are small leading to reduced waste accumulation, while the short residence times reduce solvent degradation. The small processing volumes are compensated by the high extraction efficiencies obtained. The small channel extractors

exhibited high overall mass transfer coefficients, which in comparison with conventional contactors are up to two or three orders of magnitude higher [10].

Table 1. Summary of experimental investigations of single component actinide and lanthanide extraction in microchannels.

Micro-scale device	System	Reference
Y-junction microchannel *w: 100.5 μm; d: 43.5 μm*	U(VI) HNO_3 – TBP/Kerosene	[11]
T-junction *D: 0.5-2 mm*	U(VI)	[12]
Monoblock Distributor with Integrated Microfluidic Junctions (MDIMJ)	U(VI) HNO_3 – TBP/dodecane	[13]
T-junction *D: 750 μm*	U(VI) HNO_3 – TBP/dodecane	[14]
T-junction *D: 500 μm*	U(VI) HNO3 – TBP/Ionic Liquids	[15] [16]
T-junction *D: 400 μm*	U(VI) HNO_3 – TBP/dodecane	[17]
Y-junction microreactor *(w: 130 μm d: 50 μm)*	Am(III) HNO_3 – CMPO/D80	[18]
Y-junction microchannel *w: 100 μm; d: 40 μm*	Pu(IV) HNO_3 – TBP/n-dodecane	[19]
T-junction *D: 200 μm*	Eu(III) HNO_3 – CMPO//TBP/D80	[20]
T-junction *D: 200 μm*	Eu(III) HNO_3 – CMPO//TBP/D80	[21]
Y-junction microchannel *w: 100 μm; d: 40 μm*	Nd(III) HCl - P507/sulfonated kerosene	[22]

Although there is a lot of work on the mass transfer and hydrodynamic performance of small channel devices involving aqueous solutions (e.g. nitric acid) and organic mixtures (e.g.

kerosene/TBP/CMPO) for single-component extraction, the available experimental studies for multi-component mixtures of actinides and lanthanides are limited. In Table 2, a summary of the works involving multi-component separations is presented. The main findings from these studies showed that in microfluidic channels, extraction equilibrium was quickly achieved and robust designs to handle toxic systems can be obtained by keeping the volume of the solvent low [23, 24]. The studies demonstrated effective separation between heavy and light lanthanides at low flow rate conditions [25]. In addition, it has been possible to derive reliable kinetics of the separations of multi-component mixtures because of the fast mixing in the microchannels, which can be used to optimize the design of the separator. [26]. Mathematical models have also been proposed that simulated the co-decontamination part of the PUREX process involving several radioactive components in microchannels, which showed substantial improvements in terms of cost and waste management (reduced solvent volume) compared to conventional units (air pulsed columns and mixer-settlers) [27, 28].

Table 2. Multicomponent separations in microsystems

Method and device	**Multi-component system**	**Reference**
3-stage chaotic advection microextractors	Ce(III)/Pr(III)	[23]
Microfluidic device (D=250 μm)	Am(III)/Pm(III)	[24]
Extraction chromatography in microsystems	U(VI) and Th(IV)/Eu(III)	[29]
Solid phase extraction – Microcolumn device	U(VI) and Pu(IV) from trace metals	[30]
Centrifugal microfluidic platforms	U(VI)/Eu(III)	[31]
Microfluidic device (D=150 μm)	Mixture of all lanthanides	[26]
Microchannel w:100μm; d:100μm	Pr(III)/Nd(III) and Pr(III)/Sm(III)	[25]

At the moment, small channel separations can find applications in the analysis of nuclear waste to identify the best safety routes for waste disposal, or for fast and safe assessment of newly developed ligands. In general, the adoption of intensified separations in small channels by

industry is limited mainly by the volume of the material that can be processed. To increase throughput, scale-up, scale-out and a combination of both approaches should be considered. Regarding scale-up, larger channels should be considered up to sizes that preserve the benefits of operating in small scales [32]. Scale-out is based on the concept of many equal size channels operating in parallel at similar conditions. For effective scale-out, robust manifold designs should be developed that are mechanically easy to operate and ensure that flow distribution can be controlled for a wide range of conditions [33].

In this work, we investigate experimentally and numerically the separation of U(VI) from a multicomponent mixture of an actinide and a heavy lanthanide, i.e. U(VI)/Er(III) in small channels. The separation of lanthanides from actinides is essential for the spent fuel recycling, since lanthanides in the fuel compete with actinides for neutrons and limit the efficiency of both thermal and fast reactors. In addition, risk of supply makes the recovery of Er(III), and heavy lanthanides in general, important. The mass transfer performance and flow characteristics were analysed during plug flow in small channels for different physical properties of the phases (viscosity, interfacial tension) and operating conditions (flow rates, flow rate ratio, extractant concentration, residence time). The effect of increasing the channel size from 1 to 3 mm ID on mass transfer was investigated. The experimental results on mass transfer were compared against the predictions of a two-dimensional computational fluid dynamics (CFD) model, which uses as an input the experimental concentrations at one axial location of the channel.

2. Materials, experimental setup and procedure

2.1 Materials

Uranyl nitrate hexahydrate ($UO_2(NO_3)_2 \cdot 6H_2O$) and erbium nitrate pentahydrate ($Er(NO_3)_3 \cdot 5H_2O$) were dissolved in nitric acid solutions (aqueous phase). The organic phase was a mixture of Exxsol D80 and tributylphosphate [TBP; $O=P(OC_4H_9)_3$], as the extractant of the metal ions, at different volume concentrations (70:30, 35:65, 0:100).

2.2 Experimental setup and procedure

A schematic of the experimental setup for the continuous extraction and hydrodynamics experiments is shown in Fig. 1. Two high-precision pumps (Harvard PHD Ultra) were used to feed the two phases into the test channel. The two phases were introduced into the small channels via a T-junction where they mixed. The organic phase was delivered in the T-junction

on the same axis as the test section, while the aqueous phase was delivered perpendicularly to it. The test section and the T-junction were made of FEP tubing with all branches of the T-junction having the same internal diameter as the test section. To investigate the effect of the residence time, the test section length was adjusted while the flowrates of the two phases remained the same, to ensure that the flow pattern and the mixing did not change. At the end of the test channel, a flow separator (Zaiput Ltd) was used to fully separate the two phases. The nitric acid samples were then analysed using a UV-Vis spectrophotometer (USB2000+ Ocean Optics), which measured the concentration of dioxouranium (UO_2^{+2}) and erbium (Er(III) metal ions. To investigate the hydrodynamic features of the two-phase system, a CMOS high-speed camera was used (V1212 Phantom) with maximum resolution of 1280 × 8000 12600 fps, equipped with a magnification lens (× 12, LEICA Monozoom 7 optical system). Different magnifications were used depending on the channel size, and the pixel size of the acquired images varied from 3.75 to 9.85 μm. The plug formation time (p.f.t.) was obtained from images of the forming drops taken in the T-junction. Results were also compared with calculating p.f.t. from the number of plugs over time in the middle of the channel, and calculations agreed with less than 1% deviation. For each set of conditions, the concentrations were measured a number of times to ensure that the standard deviation of 3 consecutive measurements was below 3%. In addition, experiments were conducted 3 times for each set of conditions and an average value was used for the design of experiments (see section 2.3). This resulted to an average error of 3% for the estimation of the extraction in the channel. For all extraction experiments, the initial concentration of U(VI) and Er(III) in the aqueous nitric acid solution was 22 mol/m^3 and 71 mol/m^3, respectively.

Equilibrium extraction experiments were performed to obtain the distribution coefficients (D_i) for different TBP concentrations in the organic phase and nitric acid concentrations in the aqueous phase. For these studies, the aqueous nitric acid solution with different U(VI) and Er(III) concentrations, was mixed with an appropriate volume (depending on the phase ratio used in the flow experiments) of the organic phase in a beaker with a mechanical stirrer until equilibrium was reached (3 h). The average error on the measurement of the extraction was 2%.

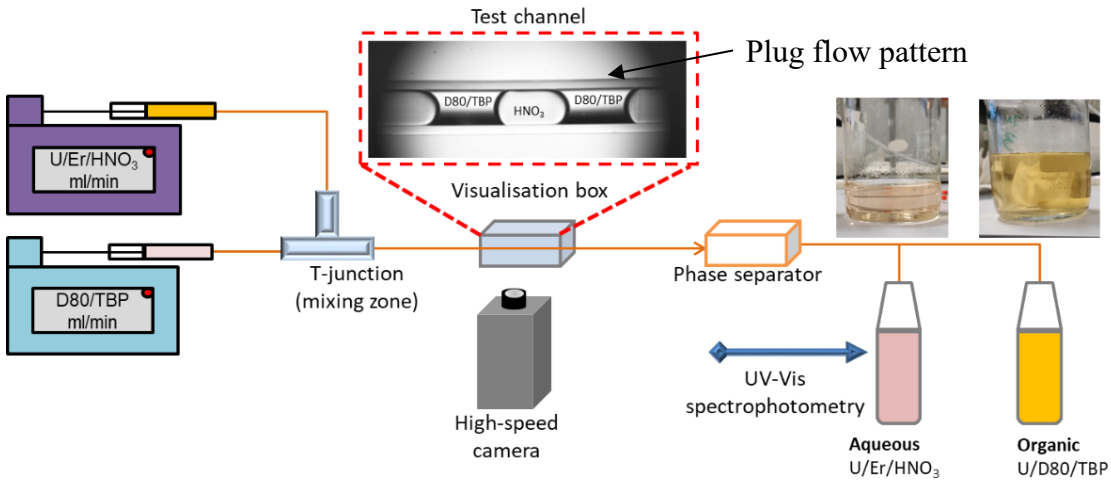

Figure 1. Schematic of the experimental setup.

2.3 Design of experiments

The mass transfer of the metal ions in the small channels was studied during plug flow. Mass transfer depends on the operating conditions and the hydrodynamic features of this flow pattern. The effects of different independent variables on extraction percentage, interfacial area and plug formation time, as shown in Table 3, were analysed, for constant nitric acid concentration of 3 M. The relationship between the responses (extraction percentage, interfacial area and plug formation time) and the independent variables (Table 3) was obtained through the Response Surface Method (RSM) [34].

Table 3. Range of values for the independent variables.

Independent Variables	Range
Channel Diameter, D (mm)	1-3
Extractant (TBP) concentration (% v/v)	30-100
Q_{org}/Q_{aq}	0.5-1
Residence time, t (s)	5-20
Mixture velocity, u_{mix} *(m/s)*	0.05-0.3
Organic (aqueous) flowrate (mL/min)	0.24-3.18 (0.24-4.24)
HNO_3 *(M)*	1-3

For the evaluation of the extraction percentage the independent variables were 4, i.e. channel diameter, TBP concentration in the organic phase, phase flow rate ratio (Q_{org}/Q_{aq}), and

residence time. For the evaluation of interfacial area and plug formation time, the independent variables were 3, i.e. channel diameter, TBP concentration, and phase flow rate ratio (Q_{org}/Q_{aq}). In Table 4, the actual and coded values for the independent variables are shown. For the study of the extraction performance, a Box-Behnken design was used to assess the effects and interactions of the independent variables on the response (see Table A in Appendix). The evaluation of the interfacial area and plug formation time was performed in the same way by using a Box-Behnken design with three independent variables and three levels (as shown in Table 4).

Table 4. Actual and coded values of independent variables.

Coded values	**Actual values**			
	TBP (% v/v)	Q_{org}/Q_{aq}	*D (mm)*	*t (s)*
-1	30	0.5	1	5
0	65	0.75	2	12.5
1	100	1	3	20

The relationship between responses and the independent variables was expressed by a quadratic polynomial model according to the following equation:

$$Y = \beta_0 + \sum_{i=1}^{k} \beta_i X_i + \sum_{i=1}^{k} \beta_{ii} X_i^2 + \sum_i \sum_j^k X_i X_j \beta_{ij} + \varepsilon \quad (1)$$

where Y represents the response (one of extraction percentage, plug formation time, and specific interfacial area), X_i and X_j indicate the independent variables and k is the number of independent variables. In addition, β_0 is a constant, β_i is the coefficient of linear parameters, β_{ii} is the coefficient of quadratic parameters, β_{ij} is the coefficient of crossed parameters, which represents the interactions between the independent variables, and ε is the residual error associated to the experiments. The regression relationship was calculated by the least-squares method using the Minitab 17 software. Analysis of variance was employed to determine the validity of the models, and in Table 6, the P-Values for each term and the coefficients of determination, i.e. R^2 and $R^2_{(predicted)}$ are listed. Statistical significance was determined at 95% of confidence level. P-Values less than 0.05 mean that the term is significant for the model, while values greater than 0.05 mean that the term does not have significant impact on the model (see Table B in appendix). The final equations for the three responses are shown in Eqs. (2) - (4). The coefficients of determination show good agreement between the model and the

experimental results as well as good predictive capability of new observations within the ranges investigated. A parity plot of the distribution of the experimental and the predicted values for the extraction percentage is shown in Appendix (Figure A).

$$\mathbf{E\%}=-16.2+0.254\cdot TBP+ 131(Q_{org}/Q_{aq})-14\cdot D+3.66\cdot t-74.7\cdot(Q_{org}/Q_{aq})^2-0.065\cdot t^2+ 0.098\cdot TBP\cdot D- 0.014\cdot TBP\cdot t \quad (2)$$

$$\mathbf{p.f.t.}=1.115+ 0.001\cdot TBP-1.157\cdot(Q_{org}/Q_{aq})-0.429\cdot D+ 0.586\cdot(Q_{org}/Q_{aq})^2+ 0.1685\cdot D^2-0.001\cdot TBP\cdot D \quad (3)$$

$$\boldsymbol{\alpha}=5362+2.82\cdot TBP -1424\cdot(Q_{org}/Q_{aq})-2531\cdot D -0.032\cdot TBP^2+361.4\cdot D^2+388.6\cdot(Q_{org}/Q_{aq})\cdot D \quad (4)$$

3. Results and discussion

3.1 Equilibrium extraction

An important contribution of this study was to identify the parameters that mostly affect the extractions, since there are many variables that affect the system. The initial equilibrium studies showed the effect of nitric acid and TBP concentrations on the extraction percentage of UO_2^{+2}. The equilibrium extraction percentage, E_{eq} (%), and the distribution coefficient of UO_2^{+2} (D_U) are calculated as follows:

$$E_{eq} = \frac{C_{aq,init} - C_{aq,eq}}{C_{aq,init}} \quad (5)$$

$$D_U = \frac{C_{org,eq}}{C_{aq,eq}} \quad (6)$$

where $C_{aq,init}$ is the initial concentration of UO_2^{+2} in the aqueous phase, and $C_{org,eq}$ and $C_{aq,eq}$ are the concentrations of UO_2^{+2} in the organic and aqueous phases at equilibrium, respectively. The results are shown in Fig. 2 as a function of TBP concentration.

Erbium(III) was not extracted by TBP to the organic phase, and its values are not shown in the graph since they were within the experimental error of the UV-Vis measurements. As it can be seen, both equilibrium extraction and distribution coefficient increase by increasing TBP concentration. In addition, results show that the presence of erbium(III) did not affect the extraction of uranium(VI), since similar values were obtained for both the single and the multicomponent separations. As can be seen in Fig. 3, the amount of UO_2^{+2} ions extracted in the organic phase is slightly increased with the nitric acid concentration in the aqueous phase. The differences in extraction for the various nitric acid concentrations are larger than the 2% experimental error.

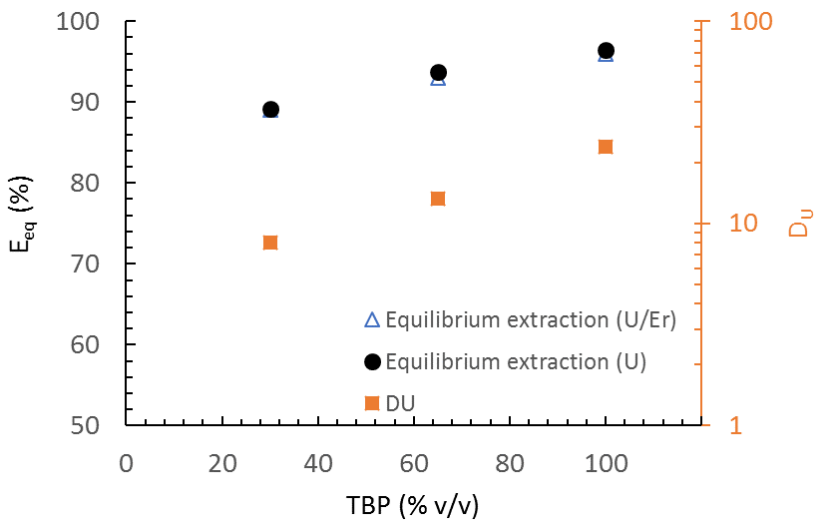

Figure 2. Single and multi-component equilibrium extraction of UO_2^{+2} ions from the 3 M nitric acid solution. (Concentrations of U(VI) and Er(III) in the initial aqueous nitric acid solutions were 22 mol/m^3 and 71 mol/m^3 respectively). D_U axis in logarithmic scale.

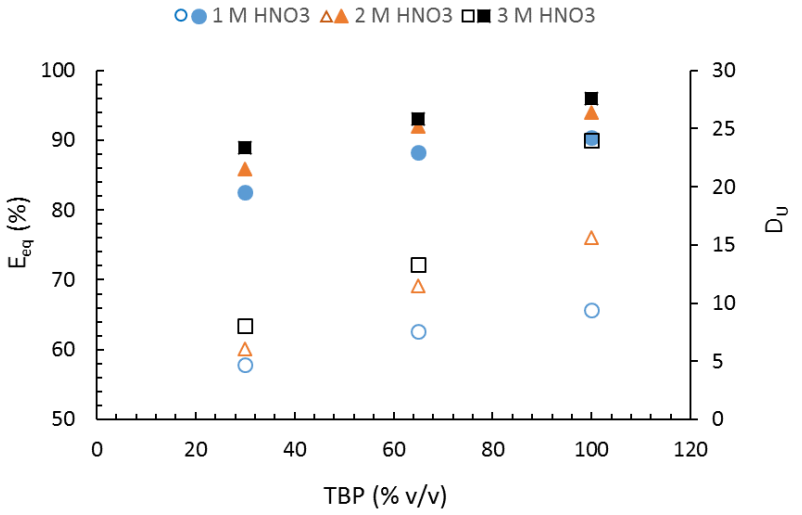

Figure 3. Equilibrium extraction of UO_2^{+2} ions from a U(VI)/Er(III) mixture in nitric acid solutions as a function of TBP concentrations, at different nitric acid concentrations. Empty symbols correspond to the distribution coefficient values at different nitric acid concentrations.

3.2 Continuous extraction in small channels – Effects of interacting independent variables on extraction

Following the equilibrium experiments, the effect of the independent variables shown in Table 3, on the mass transfer performance of the continuous small channel extractors during plug flow was investigated. The mass transfer of UO_2^{+2} ions between the two phases occurs during

the initial mixing in the T-junction inlet and subsequently during the plug flow along the channel. Therefore, to analyse the mass transfer results it is crucial to relate them to the hydrodynamic features of the plug flow pattern such as 1) the plug formation time, which is related to the mixing time in the T-junction, and 2) the interfacial area available for mass transfer during flow in the channel.

The effects of the different parameters on the extraction of UO_2^{+2} ions are summarised in Fig. 4. The effects of the independent variables on the plug formation time and the interfacial area are shown in Figs. 5 and 6 respectively. In Fig. 4a, the effect of mixture velocity, u_{mix}, for two different channel sizes, i.e. 2 and 3 mm, is shown for a constant residence time (t= 20 s). As can be seen, an increase in the mixture velocity increased the extraction percentage for both channel sizes, due to the faster internal circulations in the plugs and slugs, while the plug formation time decreases (Fig. 5a) and the specific interfacial area is not affected largely (Fig. 6b). In addition, it can be observed that the effect of mixture velocity is more pronounced at low mixture velocities, whilst for mixture velocities above 0.01 m/s the extraction percentage does not change significantly. The increase in extraction percentage is larger in the 2 mm channel, attributed to the shorter diffusion lengths once the plug is formed and the faster internal circulations in the plugs and the slugs as the channel size decreases [35]. However, at the low mixture velocity (u_{mix}=0.005 m/s), the extraction in both 2 and 3 mm channels is similar. This is attributed to the fact that the plug formation time in the 3 mm channel is much longer than in the 2 mm one, (Fig. 5a), allowing significant mass transfer in the mixing zone. The increased mass transfer in the mixing zone for the 3 mm channel compensates for the slower mass transfer due to circulation along the rest of the channel, and the lower specific interfacial area (Fig 6a), compared to the 2mm channel. A residence time of 20 s was used, because the extraction has reached a “slow rate” region, as can be seen from Figs 4c and 4d.

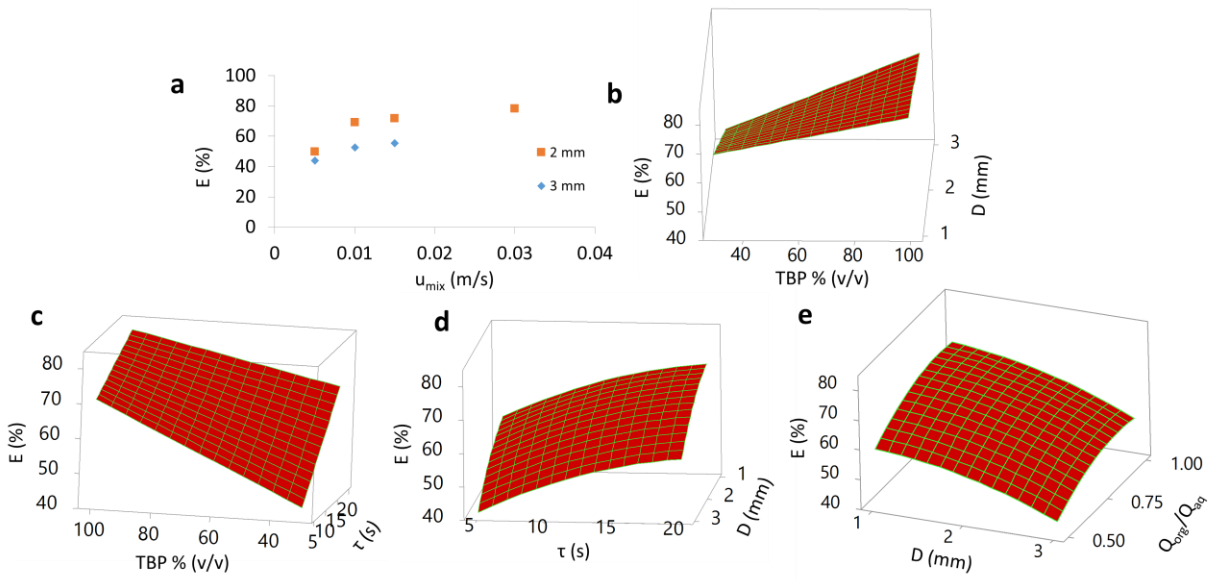

Figure 4. a) Extraction percentage of UO_2^{+2} ions as a function of mixture velocity for two different channel sizes, i.e. 2 and 3 mm (TBP=30% v/v, HNO_3=3 M, t=20 s, Q_{org}/Q_{aq}=1); **b-e)** Surface plot of extraction percentage of UO_2^{+2} ions as a function of TBP concentration, channel size, Q_{org}/Q_{aq}, and residence time at mixture velocity, u_{mix}=0.015 m/s. Constant values: **b)** Q_{org}/Q_{aq}=1, t=12.5 s, **c)** Q_{org}/Q_{aq}=1, D=2 mm, **d)** Q_{org}/Q_{aq}=0.75, TBP=65%, **e)** TBP=65%, t=12.5.

The effects of the rest of the parameters (as listed in Table 1) are presented in Figs 4b to 4e at a constant mixture velocity of 0.015 m/s. In general, it can be observed that the most dominant parameter is the TBP concentration, followed by the channel diameter and the residence time; the organic-to-aqueous phase flow rate ratio has the smallest effect on the extraction performance. It was observed (Figs 4b and 4c) that an increase in the concentration of TBP increased the extraction of UO_2^{+2} in a similar way to the equilibrium results shown in Fig. 2. At equilibrium, an increase of the TBP concentration from 30% to 100% (pure TBP), increases the extraction percentage by ~5.5%. However, in the continuous contactors, the impact of TBP concentration in the extraction percentage is also affected by the other factors and the extraction percentage varied from 8% to 40%. This large variation between 30 and 100% (v/v) TBP, especially at short residence times, compared to the equilibrium results, cannot be explained by changes in hydrodynamic properties; at a certain channel size, both plug formation time (Fig. 5c) and interfacial area (Fig. 6d) show little dependence on the TBP concentration. For example in the case of 1 mm, the plug formation time decreases (~10%) by increasing the TBP concentration from 30% to 100% (v/v) TBP, which means less contact time in the mixing zone,

whilst the specific interfacial area increases only by 5.7%. It is possible that the differences in extraction observed between the two TBP concentrations are due to the different uranyl complexes formed at different TBP concentrations [36]. Molecular dynamic studies on the transfer of uranyl ions from an aqueous (nitric acid) into an organic (TBP/kerosene) phase have suggested that migration proceeds in the form of different complexes, i.e. $UO_2(NO_3)_x \cdot nH2O \cdot kTBP$ where x, n, k ϵ {1, 5} [37-39], before a final state is reached. Depending on the conditions (such as nitric acid concentration, uranyl concentration, TBP concentration, water content) the uranyl complexes undergo structural reformation and chemical composition changes (changes in hydrophobicity) to accommodate the migration from the aqueous into the organic phase. More specifically, an increase at TBP concentration favours the formation of uranyl complexes hydrophobic in nature and creates a more favourable environment for their extraction to the bulk organic phase. This can also explain the fact that as the concentration of TBP increases, the impact of the channel size on the extraction percentage decreases (Fig. 4b). In the case of 100% TBP, where mostly hydrophobic complexes form, the better mixing in the smaller channel does not have the same impact as in the case of 30% TBP. At 30% TBP, the extraction percentage decreases by ~34% by increasing the channel size from 1 to 3 mm, whist at 100% the decrease is ~14%.

It is worth mentioning that the results shown in Fig. 4b are for constant residence time 12.5 s, just before the extraction percentage reaches a plateau (Fig. 4d). The interaction of TBP and residence time is shown more clearly in Fig. 4c, where a high dependence on residence time is observed at low TBP concentration, whilst as the TBP concentration increases the effect of residence time decreases. Similarly, as the residence time increases from 5 to 20 s, the effect of TBP concentration decreases. As expected, the increase of residence time has a positive effect on the extraction percentage for all channel sizes (Figs. 4c and 4d). After approximately 12.5 s, in all channels, the extraction percentage continues to increase, but at a slower rate, until equilibrium is reached.

In Fig. 4e, the effects of organic-to-aqueous phase flow rate ratio and channel size at constant residence time and TBP concentration are shown. For all channel sizes, the extraction percentage increases by increasing the Q_{org}/Q_{aq} ratio, since more solvent is used. However, the extraction percentage for phase ratios 0.75 and 1 is similar, indicating that comparable extractions can be achieved by using less solvent or more aqueous phase. This is attributed to the fact that when the amount of solvent used decreases with decreased phase flow rate ratio

(at constant mixture velocity), the plug formation time (Figs. 5b and 5d) and the specific interfacial area (Figs. 6c and 6e) increase, favouring mixing and interfacial mass transfer.

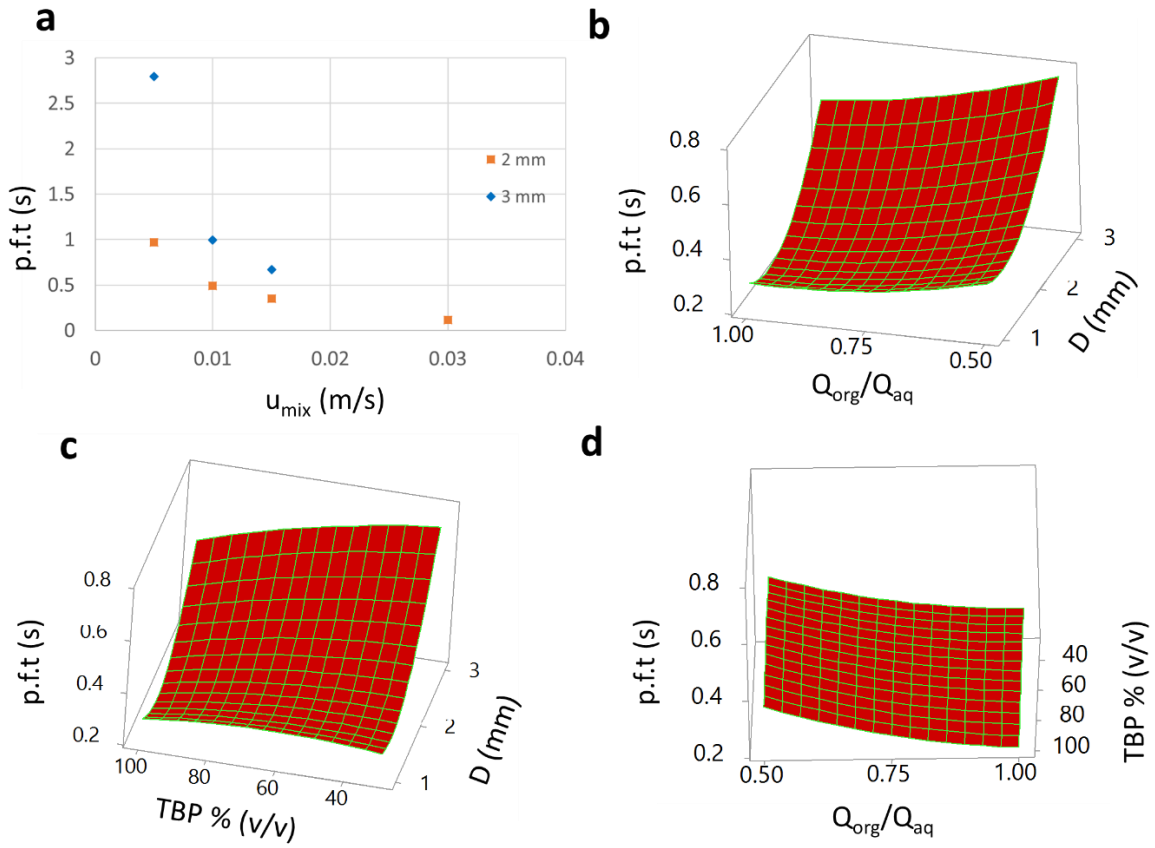

Figure 5. a) Plug formation time (p.f.t) as a function of mixture velocity (Q_{org}/Q_{aq}=1, TBP=30% v/v), **b-d)** Surface plots of plug formation time as a function of TBP concentration, channel size, and Q_{org}/Q_{aq} at mixture velocity, u_{mix}=0.015 m/s. Constant values: **b)** TBP=65% v/v, **c)** Q_{org}/Q_{aq}=0.75, **d)** D=2 mm.

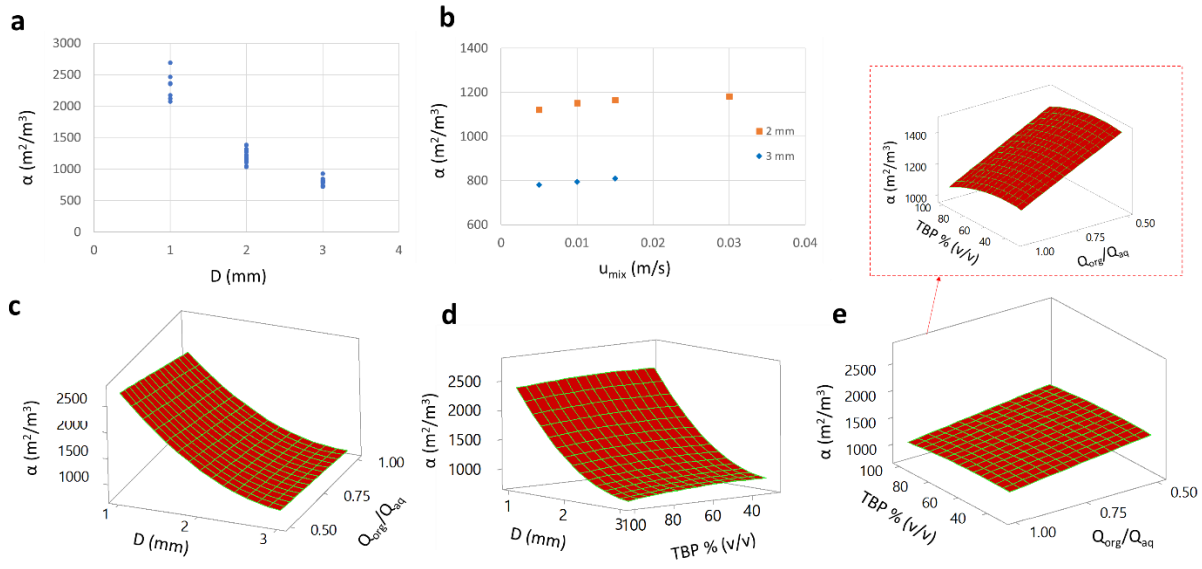

Figure 6. a) Specific interfacial area (α) as a function of channel size for all conditions investigated, **b)** Specific interfacial area as a function of mixture velocity (Q_{org}/Q_{aq}=1, TBP=30% v/v), **c-e)** Surface plots of specific interfacial area as a function of TBP concentration, channel size, and Q_{org}/Q_{aq} at mixture velocity, u_{mix}=0.015 m/s. Constant values: **c)** TBP=65% v/v, **d)** Q_{org}/Q_{aq}=0.75, **e)** D=2 mm.

3.3 Overall mass transfer coefficients ($k_L\alpha$)

The overall mass transfer coefficients for the continuous extraction in the small channels can be calculated from the experimental concentrations. The rate of mass transfer of UO_2^{+2} ions from the aqueous phase to the organic phase is given by:

$$\frac{dC_{aq}}{dt} = -k_L\alpha\,(C_{aq} - C_{aq,eq}) \qquad (7)$$

where C_{aq} is the concentration of the UO_2^{+2} ions in the bulk aqueous phase (at time t_i), and $C_{aq,eq}$ is the concentration of the UO_2^{+2} ions in the aqueous phase at equilibrium with the organic phase at infinite time ($t=\infty$). $C_{aq,eq}$ was measured experimentally for the different volume ratios of the phases used in this work as described in Section 2.3.

By integrating Eq. (7), Eq. (8) is obtained:

$$\int_{C_{aq,t_a}}^{C_{aq,t_b}} \frac{1}{(C_{aq}-C_{aq,eq})}\,dC_{aq} = -k_L\alpha \int_{t_a}^{t_b} dt \qquad (8)$$

Eq. (8) can be integrated for different time intervals, i.e. t_a to t_b, that can span from the initial contact time of the two phases in the mixing zone (where time is 0) to a time further

downstream the channel. The latter is calculated for different channel lengths by dividing the total flowrate with the channel volume. C_{aq,t_a} is the initial concentration in the aqueous phase and C_{aq,t_b}, is the concentration at time t_b. The overall volumetric mass transfer coefficient can then be found as follows:

$$k_L\alpha = \frac{1}{t_b - t_a} \ln\left(\frac{C_{aq,eq} - C_{aq,t_a}}{C_{aq,eq} - C_{aq,t_b}}\right) \quad (9)$$

In Fig. 7, the overall mass transfer coefficients are plotted against the residence time. The mass transfer coefficients are calculated including the mixing zone (T-junction). It can be seen that the overall mass transfer coefficient for the entire extractor decreases as the channel size and the residence time increase and the values range from 0.05 to 0.24 s^{-1}. These results demonstrate that for short residence times, smaller channels have better mass transfer performance. The mass transfer coefficients are one to three orders of magnitude larger than in other types of contactors typically used for similar actinide extractions [40].

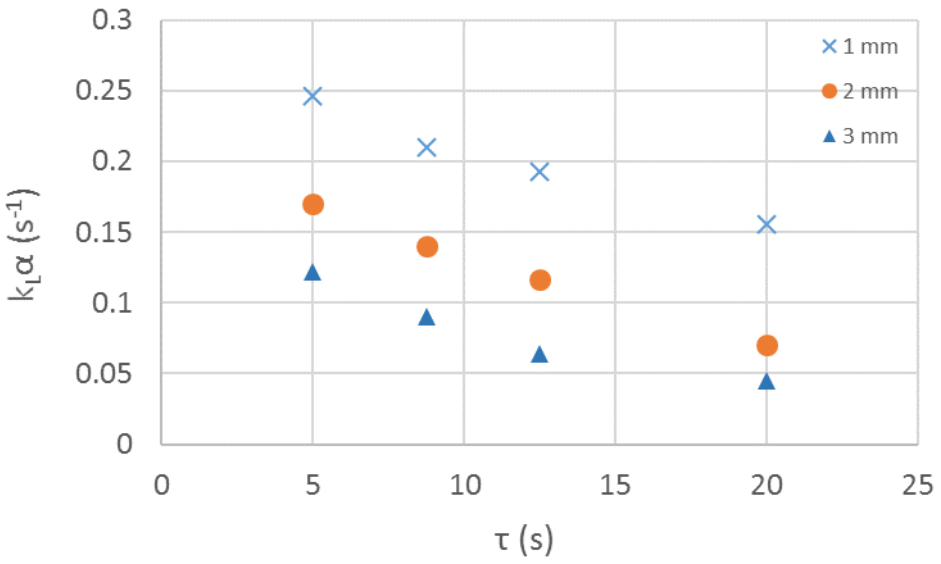

Figure 7. Overall mass transfer coefficient as a function of the residence time for the 3 different channel sizes (TBP=30% v/v, Q_{org}/Q_{aq}=1, u_{mix}=0.01 m/s).

3.4 Evaluation of the effect of the mixing zone

To isolate the effect of the mixing zone (T-junction inlet) on the overall mass transfer performance, t_a was chosen at a position further downstream from the inlet, where the plug flow was fully developed. Residence times that give extraction percentages between 40–80% were chosen. This range ensured that at the low end, the amount of extraction was larger than

the one in the mixing region, while at the high end it is not approaching the equilibrium values, where changes in the residence time have only a small effect on extraction. For each channel size, the final concentration was measured at 4 different residence times (acquired by using different channel lengths), i.e. 5, 8.75, 12.5, and 20 s, as shown in Fig. 8a. By fitting the experimental results for the amount of UO_2^{+2} extracted (shown in Fig. 8a) to Eq. (9), the mass transfer coefficients for different time intervals can be calculated. In Table 5, the mass transfer coefficients for the different time intervals are presented and, as expected, the mass transfer coefficient remains almost constant for each channel size. At residence time 20 s, the extraction for the 1 mm channel was approaching equilibrium and the results have not been included.

Table 5. Mass transfer coefficient for different time intervals.

Time interval (s)	**$k_L\alpha$ (s^{-1})**		
($t_a \rightarrow t_b$)	**1 mm**	**2 mm**	**3 mm**
5-8.75	0.139	0.054	0.024
5-12.5	0.141	0.052	0.025
8.75-12.5	0.140	0.052	0.024
5-20	-	0.048	0.022
8.75-20	-	0.048	0.023
12.5-20	-	0.049	0.023
Average $k_L\alpha$	**0.140**	**0.051**	**0.024**

As can be seen from Fig. 8b, the experimental concentrations at the various residence times are predicted well using the averaged $k_L\alpha$ (Table 5), with an average absolute error of 2 %. To evaluate the effect of the mixing zone on the extraction performance, Eq. (10), derived from Eq. (9), is solved for t_a equal to the plug formation time as shown in Fig. 5. In this case, t_b and C_{aq,t_b} can be any of the downstream experimental points (Fig. 8).

$$C_{aq,t_a} = C_{aq,eq} + (C_{aq,eq} - C_{aq,t_b})e^{-k_L\alpha(t_b - t_a)} \quad (10)$$

C_{aq,t_a} corresponds to the concentration in the aqueous plug after the T-inlet mixing zone and $k_L\alpha$ is taken from Table 5. It was found that the extraction percentage in the mixing zone varied from 31-36% for the 3 different cases shown in Fig. 8.

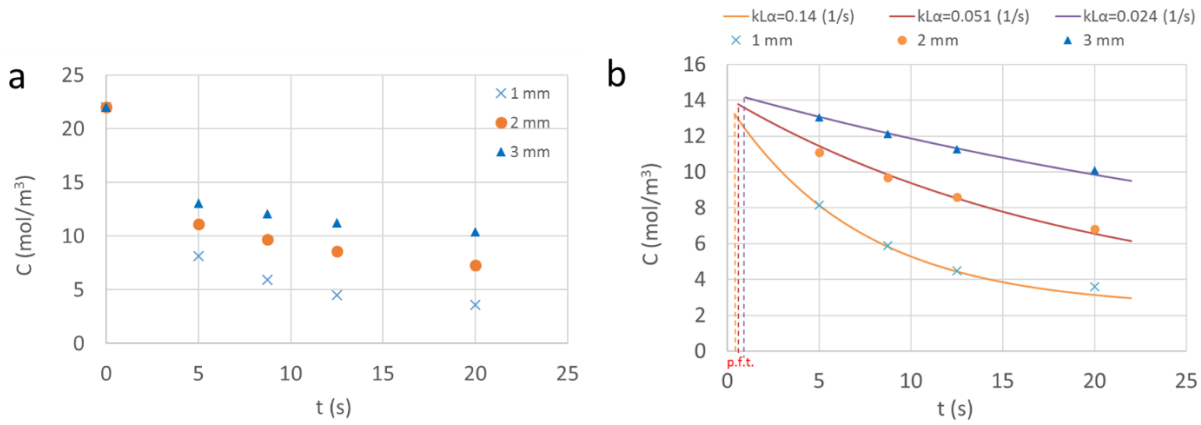

Figure 8. a) Experimental concentration of UO_2^{+2} ions and **b)** calculated concentration of UO_2^{+2} ions in the aqueous phase as a function of residence time (u_{mix}=0.01 m/s, TBP=30% v/v, HNO_3= 3 M, Q_{org}/Q_{aq}=1).

3.5 Use of numerical modelling to predict extraction

A computational fluid dynamics (CFD) model was developed to simulate the separation of U(VI) from Er(III) in the two-phase system during plug flow in small channels. For the simulations, a unit cell, comprised of one dispersed aqueous phase (3M HNO_3 solution) plug and one continuous organic phase (D80/TBP) slug in axisymmetric cylindrical coordinates, was used (for details see [12, 41]). All simulations were performed with a commercial finite element software (Comsol Multiphysics). The Navier-Stokes and continuity equations (Eqs. 11 and 12) for both phases were solved in steady-state to establish the velocity and pressure profiles. Subsequently, the convection-diffusion equation (Eq. 13) in both phases was solved in a transient manner to represent mass transfer during the movement of the plug along the channel. Both liquids are Newtonian and the flow was incompressible, whilst the effect of gravity was assumed negligible.

$$\rho(\mathbf{u}\cdot\nabla)\mathbf{u} = \nabla\cdot[-\mathrm{PI} + \mu(\nabla\mathbf{u} + (\nabla\mathbf{u})^{\mathrm{T}})] + \mathbf{F} \tag{11}$$

$$\rho\nabla\cdot\mathbf{u} = 0 \tag{12}$$

$$\frac{\partial c_i}{\partial t} + \nabla\cdot(D_i\nabla c_i + \mathbf{u}c_i) = 0 \tag{13}$$

The shape and the position of the plug in the computational domain remained fixed. To simulate the flow, the channel wall was assigned a constant axial velocity equal to the plug velocity, opposite to the flow direction (u_z=-u_p) (Fig. 9a) and the radial velocity was set to 0. Periodic boundary conditions for pressure were applied to the inlet and outlet of the

computational domain (Fig. 9a). We applied to No-slip condition and zero mass flux were taken at the channel wall. The geometric characteristics, i.e. plug and slug length, and film thickness (see Fig. B in Appendix) were taken from the experimental results, representing accurately the equilibrium state where forces are balanced. The rate of mass transfer is dependent on film thickness and plug size, since they can affect circulation in the plug, intensity of mixing and diffusion length [42]. A free triangular mesh was applied to the whole computational domain. At the interface, where the concentration gradients are steep, the grid was further refined as shown in the inset of Fig. 9a. Element sizes along the interface and the channel wall varied between 0.15 and 0.42 μm, whilst in the main domain of each phase they varied between 1.33 and 4.56 μm. Additionally, to satisfy the flux continuity at the interface and avoid large instantaneous fluxes, a boundary condition (stiff-spring method) and a step function were added to the model. Simulation results shown in Fig. 9b are for the case of the 2 mm channel (TBP=30% v/v, HNO_3=3 M, Q_{org}/Q_{aq}=1, u_{mix}=0.01 m/s, C_U=22 mol/m^3, C_{Er}=71 mol/m^3, μ_{aq}=1.07mPas, μ_{org}=2.22mPas ρ_{aq}=1370 kg/m^3, ρ_{org}=853 kg/m^3).

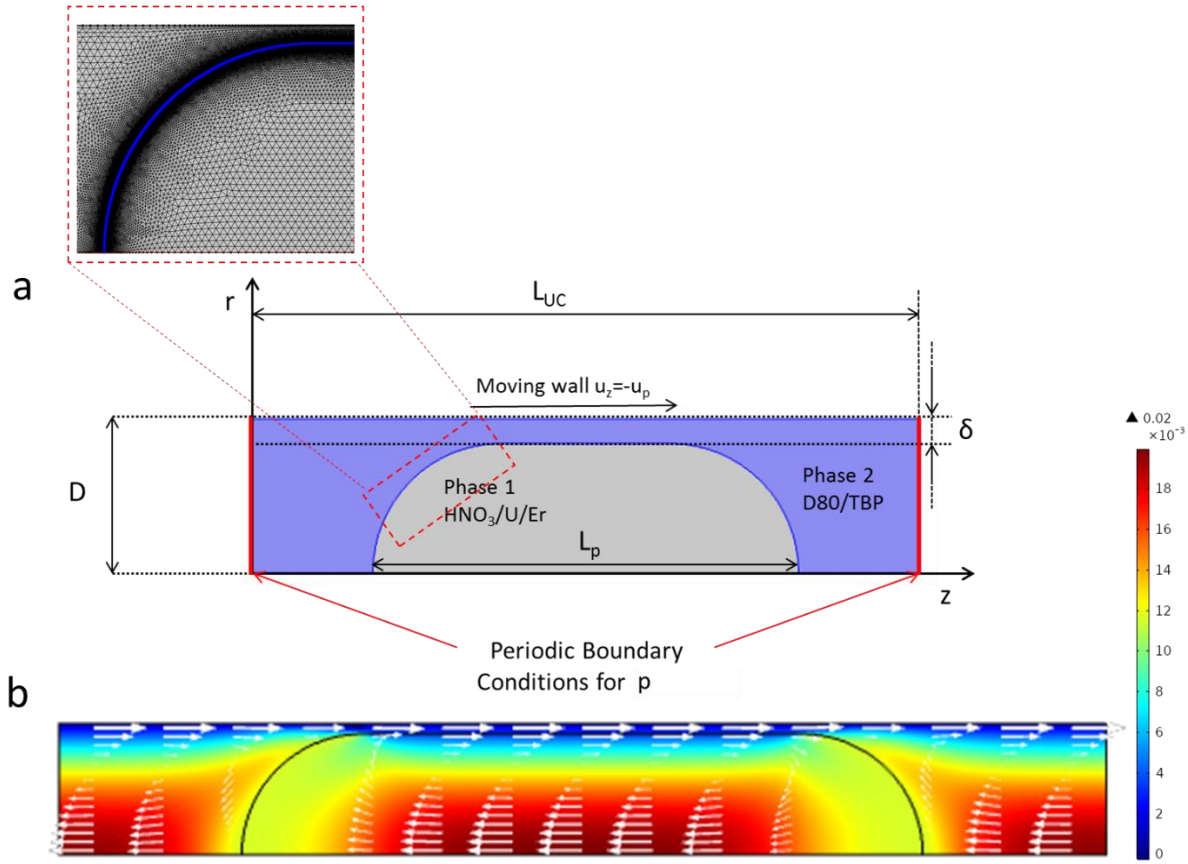

Figure 9. a) Computational domain of the unit cell under investigation; inset: grid close to the interface **b)** Velocity profile in the whole computational domain.

The diffusion coefficients of U(VI) and Er(III) in the aqueous and organic phases were taken as $D_{U,aq}=7\cdot10^{-9}$ m^2/s, $D_{U,org}=2\cdot10^{-10}$ m^2/s, $D_{Er,aq}=7\cdot10^{-9}$ m^2/s, $D_{Er,org}=10^{-10}$ m^2/s [43-45]. Three different cases were considered to compare against the experimental findings discussed in previous sections. In the first case, the initial metal concentration in phase 1 (aqueous nitric acid solution) was set equal to the feed concentration as used in the experiments (C_U=22 mol/m^3, C_{Er}=71 mol/m^3). As can be seen from Fig. 10, the simulations over-predicted the experimental concentration values, since they do not take into account the mixing in the T-junction. In the second case, the initial metal concentration in phase 1 was set equal to the value calculated from Eq. (9) for t_i equal to the plug formation time for these conditions. In the third case, the initial metal concentration of phase 1 was taken equal to the experimental result for t_i=5 s. It can be seen (Fig. 10) that for the cases where the initial concentration was taken at a time after the plug formation time, simulated and experimental results showed very close agreement (Table 6), i.e. 2.9 and 4.2% error, compared to the case where the initial concentration was taken as that of the feed solution.

Table 6. Average deviation of the CFD model from the experimental results for the different cases.

Case	Time	Concentration of UO_2^{+2} in feed (mol/m^3)	Average absolute error from exp data (%)
1	0	21	28.2
2	0.73	13.7	4.2
3	5	11.1	2.9

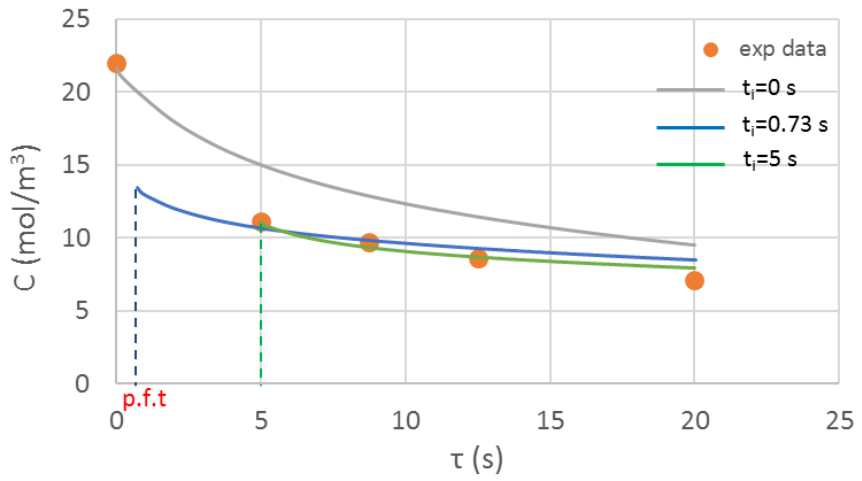

Figure 10. Experimental and CFD U(VI) concentrations in the nitric acid phase (TBP=30% v/v, HNO_3=3 M, Q_{org}/Q_{aq}=1, u_{mix}=0.01 m/s)

In Fig. 11, the concentration contours of UO_2^{+2} in the aqueous plug at different residence times are shown. The contours exhibit similar patterns to the relative velocity ones during plug flow, as shown in Fig. 9 and seen in the literature [3, 20]. The concentration contours are mainly developing within the first 2 s. The concentration profile is not uniform along the z and r coordinates, and the concentration is the highest close to the stagnation zones that are formed in the lower and upper middle part of the plug. In these zones, convective transfer of the UO_2^{+2} is absent since the fluid is not affected by circulation. The concentration reduces fast in the region close to the interphase inside the plug because of the high driving force next to the organic phase. The strong circulation current from the interface to the middle of the plug causes the concentration to reduce fast in the region along the centreline as well. In Fig. 11b, the concentration profiles at different time steps are plotted for the upper half of the plug. The concentration profiles converge at the stagnation point whose radial position is located at around 0.65 of the plug width, indicating that in the stagnation region mass transfer is very slow.

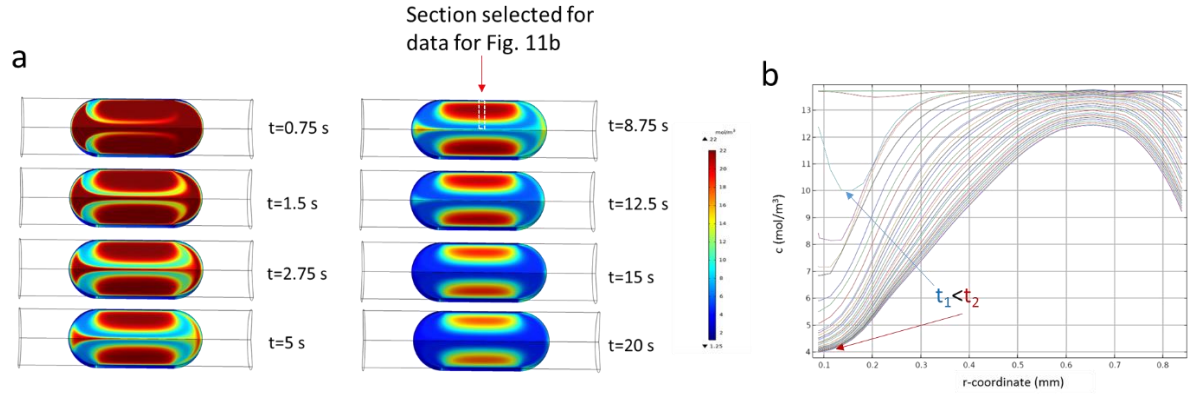

Figure 11. a) Evolution of the UO_2^{2+} concentration contours in the aqueous phase plug at different residence times, **b)** Concentration profiles (r-coordinate) at the upper half of the plug (lines represent the concentration profile at different residence times).

Conclusions

The selective separation of dioxouranium metal ions (UO_2^{+2}) from a binary U(VI)/Er(III) mixture, was investigated during liquid-liquid plug flow in small channels. The effects of different variables on mass transfer were investigated. The hydrodynamic features of the

system, i.e. plug formation time and interfacial area, were also obtained and used to understand the extraction. In general, it was found that high interfacial area to volume ratio and large plug formation time favour the extraction performance. The effects of the different variables are shown quantitatively in Table 7. Increase in TBP concentration and residence time had a positive impact on the extraction percentage, whilst an increase in the channel diameter showed the inverse trend. The large difference in extraction percentage as a function of TBP, obtained at short residence times compared to the equilibrium values, was attributed to the different uranyl complexes that are formed for different TBP concentrations. The plug formation time was mainly affected by the mixture velocity and channel size, whilst the interfacial area to volume ratio was mainly dependent on the channel size. From the plug formation time and the mass transfer results, the effect of the mixing zone on the total extraction performance of the small-scale contactor was estimated. Finally, a CFD methodology was proposed that can evaluate the mass transfer during plug flow with less than 4% error, using only one experimental point once the plug has formed.

Table 7. Qualitative representation of the impact of the different variables on the mass transfer and hydrodynamic features (red arrows represent biggest impact per response).

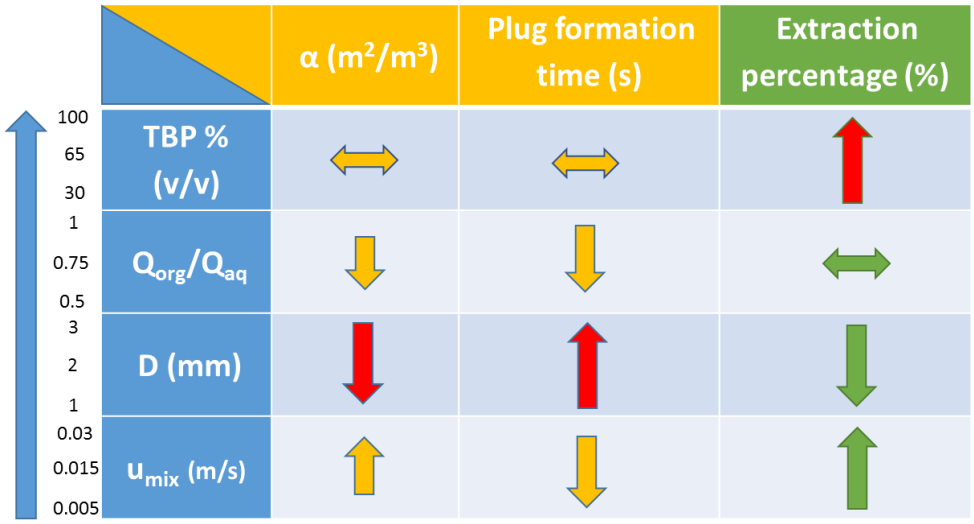

Acknowledgements

The work was supported by the EPSRC grant ATLANTIC: Accident ToLerANT fuels In reCycling (EP/S011935/1), an EPSRC grant on Feasibility Studies in Energy (EP/P034101/1), an EPSRC Impact Acceleration Account (EP/R511638/1), an Inspiration Grant (EP/K038656/1), and an EPSRC grant on Developing Innovative Radiation Measurement Technologies for Decommissioning (EP/R019223/1).

References

[1] P. Angeli, E.G. Ortega, D. Tsaoulidis, M. Earle, Intensified Liquid-Liquid Extraction Technologies in Small Channels: A Review, Johnson Matthey Technology Review 63 (2019) 299-310.
[2] D. Tsaoulidis, V. Dore, P. Angeli, N.V. Plechkova, K.R. Seddon, Flow patterns and pressure drop of ionic liquid–water two-phase flows in microchannels, International Journal of Multiphase Flow 54 (2013) 1-10.
[3] V. Dore, D. Tsaoulidis, P. Angeli, Mixing patterns in water plugs during water/ionic liquid segmented flow in microchannels, Chemical Engineering Science 80 (2012) 334-341.
[4] R. Taylor, Reprocessing and recycling of spent nuclear fuel, Woodhead Publishing Oxford, 2015.
[5] M. Carrott, C. Maher, C. Mason, M. Sarsfield, R. Taylor, “TRU-SANEX”: A variation on the EURO-GANEX and i-SANEX processes for heterogeneous recycling of actinides Np-Cm, Separation Science and Technology 51 (2016) 2198-2213.
[6] R. Taylor, M. Carrott, H. Galan, A. Geist, X. Hères, C. Maher, C. Mason, R. Malmbeck, M. Miguirditchian, G. Modolo, The EURO-GANEX process: current status of flowsheet development and process safety studies, Procedia Chemistry 21 (2016) 524-529.
[7] D.J. Kingsnorth, Rare earths: facing new challenges in the new decade, Presented by Clinton Cox, SME Annual Meeting, 2010.
[8] C. Mariet, A. Vansteene, M. Losno, J. Pellé, J.-P. Jasmin, A. Bruchet, G. Hellé, Microfluidics devices applied to radionuclides separation in acidic media for the nuclear fuel cycle, Micro and Nano Engineering 3 (2019) 7-14.
[9] T. Wang, T. Xie, C. Xu, Microextractors applied in nuclear-spent fuel reprocessing: Micro/mini plants and radiochemical analysis, Critical reviews in environmental science and technology 49 (2019) 1-31.
[10] D. Tsaoulidis, E.G. Ortega, P. Angeli, Intensified extraction of uranium (VI) in impinging-jets contactors, Chemical Engineering Journal (2018).
[11] H. Hotokezaka, Development of the innovative nuclide separation system for high-level radioactive waste using microchannel chip-extraction behavior of metal ions from aqueous phase to organic phase in microchannel, Prog. Nucl. Energy 47 (2005) 439-447.
[12] D. Tsaoulidis, P. Angeli, Effect of channel size on mass transfer during liquid–liquid plug flow in small scale extractors, Chemical Engineering Journal 262 (2015) 785-793.
[13] M. Darekar, K.K. Singh, P. Sapkale, A.K. Goswami, S. Mukhopadhyay, K.T. Shenoy, On microfluidic solvent extraction of uranium, Chemical Engineering and Processing - Process Intensification 132 (2018) 65-74.
[14] N. Sen, M. Darekar, P. Sirsat, K.K. Singh, S. Mukhopadhyay, S.R. Shirsath, K.T. Shenoy, Recovery of uranium from lean streams by extraction and direct precipitation in microchannels, Separation and Purification Technology 227 (2019) 115641.
[15] D. Tsaoulidis, V. Dore, P. Angeli, N.V. Plechkova, K.R. Seddon, Dioxouranium(VI) extraction in microchannels using ionic liquids, Chemical Engineering Journal 227 (2013) 151-157.
[16] D. Tsaoulidis, V. Dore, P. Angeli, N.V. Plechkova, K.R. Seddon, Extraction of dioxouranium(VI) in small channels using ionic liquids, Chem Eng Res Des 91 (2013) 681-687.

[17] M. Darekar, K.K. Singh, S. Mukhopadhyay, K.T. Shenoy, S.K. Ghosh, Solvent extraction in microbore tubes with UNPS–TBP in dodecane system, Separation and Purification Technology 128 (2014) 96-105.
[18] Y. Ban, Y. Kikutani, M. Tokeshi, Y. Morita, Extraction of Am (III) at the interface of organic-aqueous two-layer flow in a microchannel, Journal of nuclear science and technology 48 (2011) 1313-1318.
[19] M. Yamamoto, S. Taguchi, S. Sato, N. Surugaya, Evaluation of plutonium (IV) extraction rate between nitric acid and tri-n-butylphosphate solution using a glass chip microchannel, Journal of separation science 38 (2015) 1807-1812.
[20] P. Angeli, D. Tsaoulidis, W. Hashi Weheliye, Studies on mass transfer of europium(III) in micro-channels using a micro Laser Induced Fluorescence technique, Chemical Engineering Journal 372 (2019) 1154-1163.
[21] Q. Li, P. Angeli, Intensified Eu (III) extraction using ionic liquids in small channels, Chemical Engineering Science 143 (2016) 276-286.
[22] L. Zhang, F. Xie, S. Li, S. Yin, J. Peng, S. Ju, Solvent extraction of Nd (III) in a Y type microchannel with 2-ethylhexyl phosphoric acid-2-ethylhexyl ester, Green Processing and Synthesis 4 (2015) 3-10.
[23] T. Xie, M. Chen, C. Xu, J. Chen, High-throughput extraction and separation of Ce(III) and Pr(III) using a chaotic advection microextractor, Chemical Engineering Journal 356 (2019) 382-392.
[24] C.A. Launiere, A.V. Gelis, High Precision Droplet-Based Microfluidic Determination of Americium(III) and Lanthanide(III) Solvent Extraction Separation Kinetics, Industrial & Engineering Chemistry Research 55 (2016) 2272-2276.
[25] S. Nishihama, Y. Tajiri, K. Yoshizuka, Separation of lanthanides using micro solvent extraction system, Ars Separatoria Acta (2006) 18-26.
[26] K.P. Nichols, R.R. Pompano, L. Li, A.V. Gelis, R.F. Ismagilov, Toward mechanistic understanding of nuclear reprocessing chemistries by quantifying lanthanide solvent extraction kinetics via microfluidics with constant interfacial area and rapid mixing, Journal of the American Chemical Society 133 (2011) 15721-15729.
[27] D. Bascone, P. Angeli, E.S. Fraga, Mathematical modelling of intensified extraction for spent nuclear fuel reprocessing, Nuclear Engineering and Design 332 (2018) 162-172.
[28] D. Bascone, P. Angeli, E.S. Fraga, A modelling approach for the comparison between intensified extraction in small channels and conventional solvent extraction technologies, Chemical Engineering Science 203 (2019) 201-211.
[29] M. Losno, J. Pellé, M. Marie, I. Ferrante, R. Brennetot, S. Descroix, C. Mariet, Separation and preconcentration of actinides from concentrated nitric acid by extraction chromatography in microsystems, Talanta 185 (2018) 586-591.
[30] J. Gao, B.T. Manard, A. Castro, D.P. Montoya, N. Xu, R.M. Chamberlin, Solid-phase extraction microfluidic devices for matrix removal in trace element assay of actinide materials, Talanta 167 (2017) 8-13.
[31] A. Bruchet, V. Taniga, S. Descroix, L. Malaquin, F. Goutelard, C. Mariet, Centrifugal microfluidic platform for radiochemistry: Potentialities for the chemical analysis of nuclear spent fuels, Talanta 116 (2013) 488-494.
[32] X. Wang, Y. Wang, F. Li, L. Li, X. Ge, S. Zhang, T. Qiu, Scale-up of microreactor: Effects of hydrodynamic diameter on liquid–liquid flow and mass transfer, Chemical Engineering Science (2020) 115838.

[33] E.G. Ortega, D. Tsaoulidis, P. Angeli, Predictive model for the scale-out of small channel two-phase flow contactors, Chemical Engineering Journal 351 (2018) 589-602.
[34] A.I. Khuri, S. Mukhopadhyay, Response surface methodology, Wiley Interdisciplinary Reviews: Computational Statistics 2 (2010) 128-149.
[35] D. Tsaoulidis, P. Angeli, Effect of channel size on liquid-liquid plug flow in small channels, AIChE Journal 62 (2016) 315-324.
[36] Y.S. Fedorov, B.Y. Zilberman, A. Kopyrin, S. Arkhipov, Uranium (IV) complexes formed in extraction with tributyl phosphate from nitric acid solutions, Radiochemistry 43 (2001) 166-171.
[37] X. Ye, S. Cui, V.F. de Almeida, B.P. Hay, B. Khomami, Uranyl nitrate complex extraction into TBP/dodecane organic solutions: a molecular dynamics study, Physical Chemistry Chemical Physics 12 (2010) 15406-15409.
[38] P. Sahu, S.M. Ali, K.T. Shenoy, Passage of TBP–uranyl complexes from aqueous–organic interface to the organic phase: insights from molecular dynamics simulation, Physical Chemistry Chemical Physics 18 (2016) 23769-23784.
[39] G. Benay, G. Wipff, Liquid–Liquid Extraction of Uranyl by TBP: The TBP and Ions Models and Related Interfacial Features Revisited by MD and PMF Simulations, The Journal of Physical Chemistry B 118 (2014) 3133-3149.
[40] J.-q. Liu, S.-w. Li, Y.-y. Wang, S. Jing, Extraction of uranium nitrate with 30%(v/v) tributyl phosphate in kerosene in an pilot annular pulsed disc-and-doughnut column—Part I: Hydraulic performance, Solvent Extraction and Ion Exchange (2016).
[41] E. Garciadiego-Ortega, D. Tsaoulidis, M. Pineda, E.S. Fraga, P. Angeli, Hydrodynamics and mass transfer in segmented flow small channel contactors for uranium extraction, Chemical Engineering and Processing - Process Intensification 153 (2020) 107921.
[42] S. Ramji, A. Rakesh, S. Pushpavanam, Modelling mass transfer in liquid-liquid slug flow in a microchannel, Chemical Engineering Journal 364 (2019) 280-291.
[43] V. Friehmelt, A. He, Z. Yang, G. Marx, The diffusion coefficients and viscosities of the UO2 (NO3) 2· 2TBP complex in organic solvents, Inorganica chimica acta 111 (1986) 89-93.
[44] E. Kamio, Y. Fujiwara, M. Matsumoto, F. Valenzuela, K. Kondo, Investigation on extraction rate of lanthanides with extractant-impregnated microcapsule, Chemical Engineering Journal 139 (2008) 93-105.
[45] C. Liu, J. Shang, J.M. Zachara, Multispecies diffusion models: A study of uranyl species diffusion, Water Resources Research 47 (2011).

Appendix

Table A. Design of experiments with the Box-Behnken method (response: extraction percentage).

Nº of exp.	*TBP*	Q_{org}/Q_{aq}	*D*	*t*
1	-1	-1	0	0
2	1	-1	0	0
3	-1	1	0	0

4	1	1	0	0
5	0	0	-1	-1
6	0	0	1	-1
7	0	0	-1	1
8	0	0	1	1
9	-1	0	0	-1
10	1	0	0	-1
11	-1	0	0	1
12	1	0	0	1
13	0	-1	-1	0
14	0	1	-1	0
15	0	-1	1	0
16	0	1	1	0
17	-1	0	-1	0
18	1	0	-1	0
19	-1	0	1	0
20	1	0	1	0
21	0	-1	0	-1
22	0	1	0	-1
23	0	-1	0	1
24	0	1	0	1
25	0	0	0	0
26	0	0	0	0
27	0	0	0	0

Table B. Analysis of variance of fitted models for the 3 responses (P-Values and Coefficients of Determination).

Terms	**P-Value**		
	Extraction percentage	***Specific interfacial area***	***Plug formation time***
TBP	0.000	0.004	0.000

Q_{org}/Q_{aq}	0.049	0.000	0.000
t	0.002	N/A	N/A
D	0.004	0.000	0.000
TBP^2	0.091	0.051	0.125
$(Q_{org}/Q_{aq})^2$	0.050	0.000	0.025
t^2	0.035	N/A	N/A
D^2	0.253	0.000	0.000
TBP · (Q_{org}/Q_{aq})	0.812	0.863	0.236
TBP · t	0.046	N/A	N/A
TBP · D	0.038	0.542	0.086
(Q_{org}/Q_{aq}) · t	0.765	N/A	N/A
(Q_{org}/Q_{aq}) · D	0.235	0.002	0.112
t · D	0.213	N/A	N/A
Coefficients of determination			
R^2	86.3	97.6	98.4
$R^2_{(predicted)}$	78.6	96.2	97.4

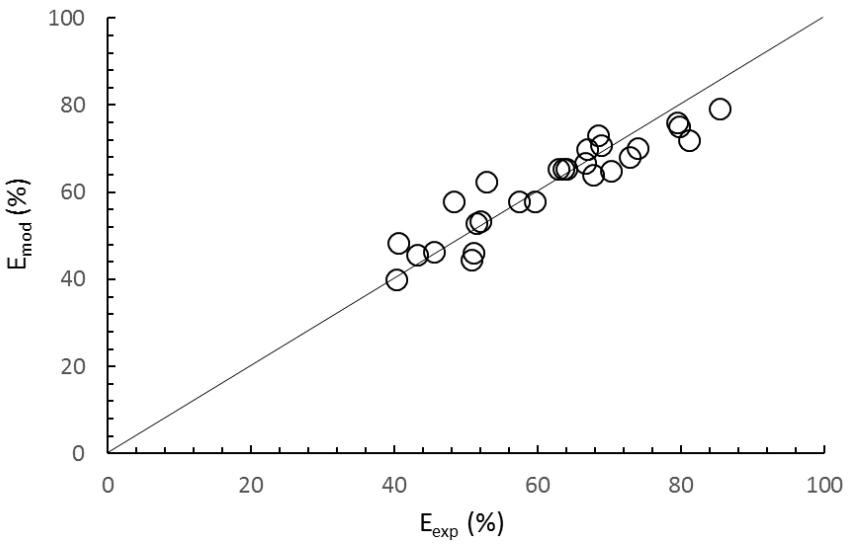

Figure A. Parity plot showing the distribution between experimental and predicted values for the extraction percentage.

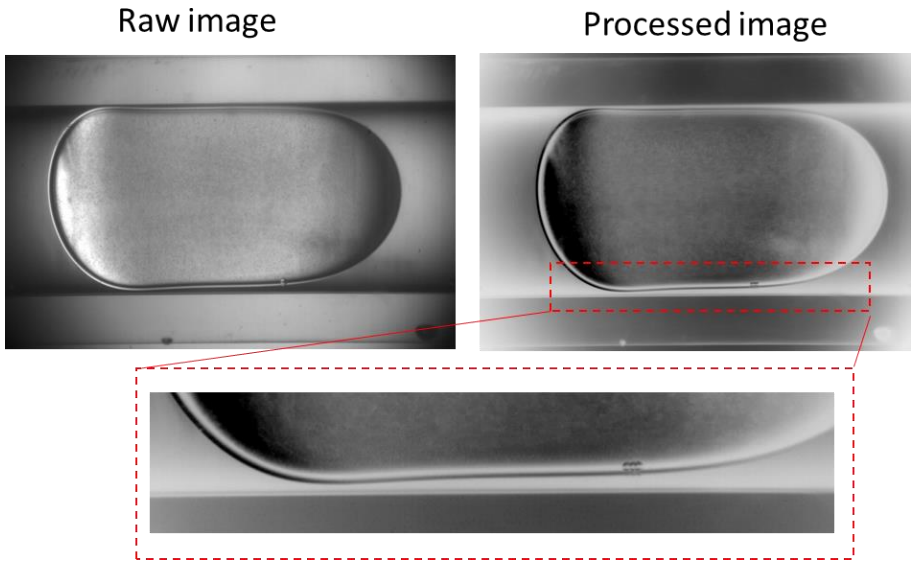

Figure B. Evaluation of the geometric characteristics (plug length and film thickness) to design the computational domain.